Folded Fabry–Perot Quasi-Optical Ring Resonator Diplexer: Theory and Experiment

HERBERT M. PICKETT AND ARTHUR E. T. CHIOU

Abstract—**Performance of folded Fabry–Perot quasi-optical ring resonator diplexers with different geometries of reflecting surfaces is investigated both theoretically and experimentally. Design of optimum surface geometry for minimum diffraction, together with the figure of merit indicating improvement in performance, are given.**

I. Introduction

A FOLDED FABRY–PEROT resonator with plane parallel reflectors, which serves the purpose of filtering the noise and diplexing the local oscillator and signal energies into the mixer, was described and tested by Gustincic [1], [2]. The basic idea is illustrated in Fig. 1. The resonator is tuned by moving the mirror block so that the local oscillator input from port I is at resonant peak of the cavity and gets transmitted into port IV. The signal input at a slightly different frequency lies in the anti-resonant band of the cavity and gets reflected from port III into port IV. The transmission characteristic of the Fabry–Perot cavity is the well-known Airy Function [3]. The advantage of the Fabry–Perot ring resonator diplexer over the two-beam interferometer diplexer [4], whose transmission characteristic is of sinusoidal nature, lies in the fact that the Fabry–Perot resonator, with the Finesse $F \gg 1$, has a better noise rejection factor for the local oscillator input port and also a much wider reflection band for the signal port. The advantage of this type of Fabry–Perot cavity over the infinite slab Fabry–Perot resonator analyzed by Arnaud *et al.* [5] and by Goldsmith [6] is that geometrical walk-off loss is eliminated. Other types of diplexers were described by Nakajima and Watanabe [7].

In Section II, we give qualitative treatment on how diffraction effect limits the performance of the diplexer and introduce a simple solution for minimum diffraction. Mathematical formulation of the problem on diplexer performance, its underlying assumptions, detailed analysis, and theoretical results are given in Section III. Some of the mathematical details are given in the Appendix. Experimental results at 100 GHz are presented in Section IV. In Section V, we conclude by summarizing our results with a description on how they can be applied to estimate the figure of merit of the diplexer with a curved reflector as compared to one with plane reflectors.

Manuscript received June 7, 1982; revised January 11, 1983. This work was supported by NASA under a contract with Caltech Jet Propulsion Laboratory.

H. M. Pickett is with the Jet Propulsion Laboratory, California Institute of Technology, Pasadena, CA 91109.

A. E. T. Chiou is with the IBM San Jose Research Laboratory, San Jose, CA.

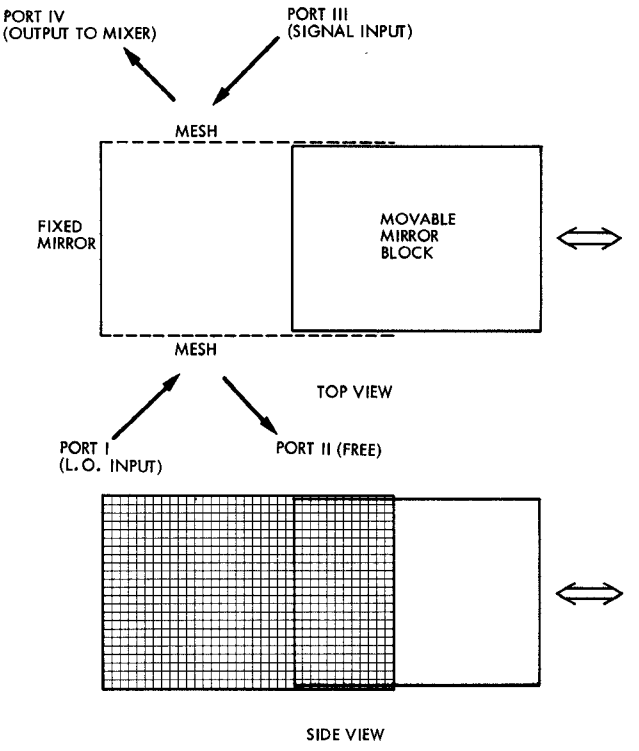

Fig. 1. Schematic diagram of a folded Fabry–Perot ring resonator diplexer.

II. Effect of Diffraction and the Related Design Problem

For applications in millimeter- and submillimeter-wave regions, performance of the diplexer is essentially limited by diffraction effects. Diffraction in the vertical direction results in energy loss of the system, since the top and bottom of the cavity are open, while diffraction in the horizontal direction couples port III and port IV together so that a significant fraction of the local oscillator input energy is distributed into port III. This can be visualized by conceptually propagating the input beam through a lattice of vertical cavities, as is illustrated in Fig. 2. Diffraction effects can be controlled by replacing one of the plane reflectors with a curved mirror with surface properly designed so as to phase match a Gaussian beam with ap-

0018-9480/83/0500-0373$01.00 ©1983 IEEE

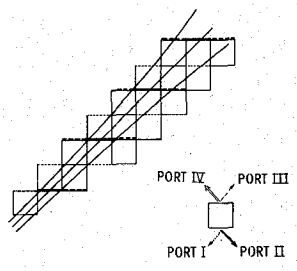

Fig. 2. Horizontal diffraction effect: a schematic illustration.

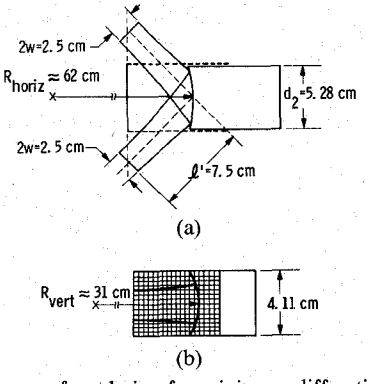

Fig. 3. Reflector surface design for minimum diffraction. (a) Top view. (b) Side view.

propriate beam waist at the plane reflector, as shown in Fig. 3. A toroidal surface with horizontal radius of curvature twice that of the vertical turns out to be a very good approximation.

Steps leading to a solution of the design problem follow.

1) Choose the free spectral range (FSR) of the cavity so that it is twice the intermediate frequency f_{IF} of the system (i.e., FSR $= 2f_{IF}$). The condition above fixes the width W and length L of the square cavity to $W = L = c/4\sqrt{2f}_{IF}$ where c is the velocity of light in free space.

2) The appropriate beam waist radius w_0 and the Raleigh length (Z_R) are given by $w_0 = W/3\sqrt{2}$, $Z_R = \pi w_0^2/\lambda$, where λ is the free-space wavelength. This choice gives a Gaussian amplitude on the mesh which has a waist parameter equal to 1/3 of the cavity width.

3) The horizontal and vertical radii of curvature for the toroidal surface are determined by $R_h = 2L + Z_R^2/L$, $R_v = R_h/2$.

Following the steps listed above, we have constructed an experimental model based on the following parameters: $f_{IF} = 1$ GHz, $W = L = 5.30$ cm, $w_0 = 1.25$ cm, $\lambda = 0.3$ cm, $R_h = 62$ cm, and $R_v = 31$ cm. In order to separate the effect of diffraction in the vertical direction from that in the horizontal direction, a resonator with a cylindrical reflector designed to control only the vertical diffraction loss has also been constructed and tested. Our experimental models also include a diplexer with plane reflectors so that the total effect of diffraction in both directions can also be observed. Preliminary experimental results were reported in [6].

Although the cavity model described above leads us to the optimum curvature with minimum diffraction effect, it is far too simple to predict how much improvement one should expect by introducing the phase-matching curved reflector. The formalism used by Arnaud *et al.* [5] can be in principle used to predict transmission of the flat-wall and curved-wall geometrices. However, the results of the walk-off analysis presented in that paper are not applicable here because of the special boundary conditions imposed by the reflecting mirrors. The flat mirror case is formally equivalent to the case treated by Arnaud if the single detector is replaced by an array of detectors. The curved mirror case is more difficult because edge diffraction from the aperture of the cavity becomes significant. Description of the cavity in terms of its resonant modes is more convenient in the high finesse case where edge diffraction is important because the effects are included implicitly. An analysis based on a modal expansion will be described in the next section.

III. Mathematical Formulation and Analysis

Exact three-dimensional analysis of performance of the diplexer with a curved reflector is fairly complicated. For practical application in the millimeter- and submillimeter-wave regions, where the curvatures are mild, we can assume that diffraction effects in the vertical and horizontal directions can be decoupled. The original problem is thus resolved into two simpler problems, namely, a one-dimensional infinite strip resonator problem for treatment of vertical diffraction loss, and a two-dimensional waveguide problem for treatment of horizontal diffraction effect. The two are decoupled in the sense that the solution from the first part enters only as a parameter into the second.

A. Infinite Strip Resonator Model

For the plane resonator diplexer, the infinite strip plane resonator model of Barone [7] is used to approximate the eigenfunction and the diffraction loss associated with each mode in the vertical direction. The excitation efficiency of each mode by various input beams (plane wave and Gaussian beams with various beam-waist sizes) is evaluated by the overlap integral of the input function and the eigenfunction of each mode. For the cylindrical and toroidal resonator diplexers, diffraction loss in the vertical direction is estimated by the infinite strip cylindrical resonator model of Boyd and Gordon [8]. Dimensions of the actual cavity and the associated models are illustrated in Fig. 4, with Fresnel Numbers and round-trip amplitude diffraction losses of the fundamental modes given in the lower part of the figure.

B. Two-Dimensional Waveguide Problem

Mathematical formulation of the two-dimensional waveguide problem, together with the appropriate coordinate system, are illustrated in Fig. 5. Dependence on the y coordinate is ignored, since the effect of field variation in the y direction was separately taken into account in Section III-A, as explained above. The electric and magnetic fields at $z = 0$ and $z = W$ can be expanded in terms of the

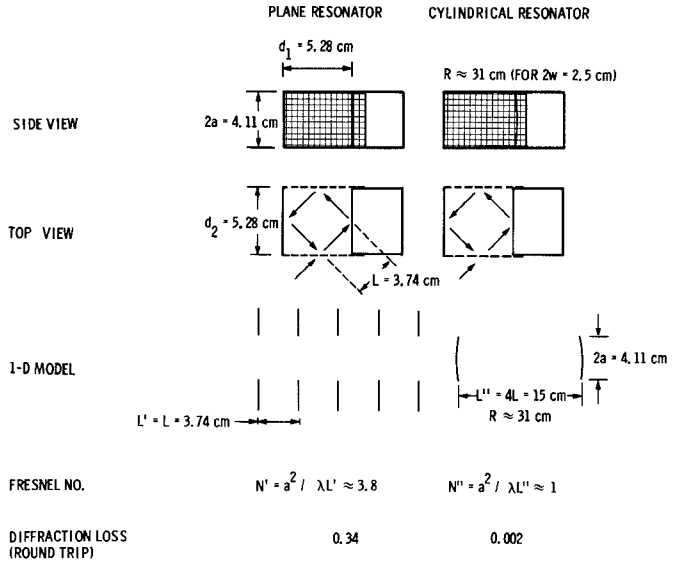

Fig. 4. Estimation of vertical diffraction loss by one-dimensional infinite strip resonator model.

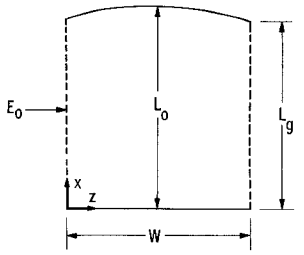

Fig. 5. Dimensions and coordinates associated with the two-dimensional waveguide analysis.

complete basis set as

$$Ey(z=0)=\sum_n e_n\sqrt{2/L_g}\sin(n\pi x/L_g) \tag{1a}$$

$$H_x(z=0)=\sum_n h_n\sqrt{2/L_g}\sin(n\pi x/L_g) \tag{1b}$$

$$E_y(z=W)=\sum_n e'_n\sqrt{2/L_g}\sin(n\pi x/L_g) \tag{1c}$$

$$H_x(z=W)=\sum_n h'_n\sqrt{2/L_g}\sin(n\pi x/L_g) \tag{1d}$$

where all the e'_n, h'_n, e_n, and h_n are complex in general.

Symbolically, we can express the expressions above as

$$\begin{pmatrix}E\\H\end{pmatrix}_{z=0}=\begin{pmatrix}e\\h\end{pmatrix} \tag{1e}$$

$$\begin{pmatrix}E\\H\end{pmatrix}_{z=W}=\begin{pmatrix}e'\\h'\end{pmatrix}. \tag{1f}$$

For an input beam linearly polarized in the y direction, we consider only the TE modes, since the TM modes are not significantly coupled to our input beam.

Presume we have a $\boldsymbol{T}$ matrix that transforms the E and M fields at $z=0$ to those at $z=W$, so that

$$\begin{pmatrix}e'\\h'\end{pmatrix}=\boldsymbol{T}\begin{pmatrix}e\\h\end{pmatrix} \tag{2}$$

the eigenvalue problem of the waveguide can then be expressed as

$$\boldsymbol{T}\boldsymbol{u}_\alpha=\Lambda_\alpha\boldsymbol{u}_\alpha=\exp(i\phi_\alpha)\boldsymbol{u}_\alpha \tag{3}$$

where $\boldsymbol{u}_\alpha$ and Λ_α are the eigenvectors and the eigenvalues of the waveguide. The procedure for determination of $\boldsymbol{T}$ matrix will be described in the Appendix.

In general, $\boldsymbol{T}$ will be a nonsymmetric real matrix and the eigenmodes will appear in pairs with eigenvalues given by $\exp(\pm i\phi)$, representing forward- and backward-going waves.

Note that if we represent the eigenvectors in the basis set as

$$u_\alpha=\begin{pmatrix}u_{1\alpha}\\u_{2\alpha}\\\vdots\end{pmatrix} \tag{4}$$

the associated eigenfunctions ψ_α will then be given by

$$\psi_\alpha=\sum_n u_{n\alpha}\sqrt{2/L_g}\sin(n\pi x/L_g). \tag{5}$$

Consider a linearly polarized input beam from port I with the electric field vector given by $\boldsymbol{E}=E_0(x)\boldsymbol{y}$ at $z=0$. If we ignore the magnetic part and also the impedance mismatch between free space and the waveguide, we can expand the incoming field in terms of the complete set of basis functions as

$$E_0(x)=\sum_n S_n\sqrt{2/L_g}\sin(nx/L_g) \tag{6}$$

where

$$S_n=\sqrt{2/L_g}\int_0^{L_g}\sin(nx/L_g)E_0(x)\,dx. \tag{7}$$

$E_0(x)$ can also be expressed in terms of the eigenfunctions as

$$E_0(x)=\sum_\alpha{}'\eta_\alpha\psi_\alpha \tag{8}$$

where the prime is used to symbolize the fact that the summation should run only over the "E-parts" of the eigenfunctions with eigenvalues representing the forward-going waves. Using (5), we can rewrite (8) as

$$E_0(x)=\sum_{\alpha n}\eta_\alpha V_{n\alpha}\sqrt{2/L_g}\sin(n\pi x/L_g) \tag{9}$$

where V is the submatrix of u which couples the E field with the forward-going eigenmodes. By comparing (6) and (9), we have

$$\sum_\alpha\eta_\alpha V_{n\alpha}=S_n \tag{10}$$

or

$$\eta_\alpha=\sum_n V^{-1}_{\alpha n}S_n. \tag{11}$$

Each eigenmode propagates independently through the Fabry–Perot, with amplitude transmittance and reflectance given by [3]

$$t_\alpha=\eta_\alpha t^2\Lambda_\alpha/(1-r^2\Lambda_\alpha^2) \tag{12a}$$

$$r_\alpha=\eta_\alpha[r+t^2\Lambda_\alpha^2/(1-r^2\Lambda_\alpha^2)] \tag{12b}$$

where r and t are the amplitude reflection coefficient and the amplitude transmission coefficient of the interfaces. From (9), (11), and (12), the total transmitted and reflected amplitudes can be expressed as

$$E_t = \sum_{\alpha nm} V_{\alpha m}^{-1} S_m V_{n\alpha} \sqrt{2/L_g} \sin(n\pi x/L_g)\left[t\Lambda_\alpha/(1-r^2\Lambda_\alpha^2)\right] \tag{13a}$$

$$E_r = \sum_{\alpha nm} V_{\alpha m}^{-1} S_m V_{n\alpha} \sqrt{2/L_g} \sin(n\pi x/L_g) \cdot \left[r + t^2\Lambda_\alpha^2/(1-r^2\Lambda_\alpha^2)\right]. \tag{13b}$$

The field E_t and E_r can be Fourier analyzed into far-field patterns. Alternatively, the amplitude received by a detector (receiver) can be determined by conceptually treating it as a transmitter and taking the overlap integral of its emitted amplitude distribution at an appropriate plane with the normalized amplitude distribution at the same plane of the field to be detected. If the detector at port IV has the same geometry as the transmitter at port I, we have, from (6) and (7)

$$E_4^* = E_0 = \sum_n S_n \sqrt{2/L_g} \sin(n\pi x/L_g) \tag{14}$$

and

$$S_n = \sqrt{2/L_g} \int_0^{L_g} E_4^* \sin(n\pi x/L_g)\, dx. \tag{15}$$

Amplitude received by the detector at port IV is then given by

$$t_4 = \int_0^{L_g} E_4^* E_t\, dx. \tag{16}$$

Using (12a), (13b), and (14), we get

$$t_4 = \sum_{\alpha nm} V_{\alpha m}^{-1} V_{n\alpha} S_m S_n \left[t^2\Lambda_\alpha/(1-r^2\Lambda_\alpha^2)\right]. \tag{17}$$

Similarly, if

$$Q_n = \sqrt{2/L_g} \int_0^{L_g} E_3^* \sin(\eta\pi x/L_g)\, dx \tag{18}$$

then

$$t_3 = \sum_{\alpha nm} V_{\alpha m}^{-1} V_{n\alpha} S_m Q_n \left[t^2\Lambda_\alpha/(1-r^2\Lambda_\alpha^2)\right]. \tag{19}$$

For port I and port II, we have

$$r_1 = \sum_{\alpha nm} V_{\alpha m}^{-1} V_{n\alpha} S_m S_n \left[r + t^2\Lambda_\alpha^2/(1-r^2\Lambda_\alpha^2)\right] \tag{20}$$

$$r_2 = \sum_{\alpha nm} V_{\alpha m}^{-1} V_{n\alpha} S_m Q_n \left[r + t^2\Lambda_\alpha^2/(1-r^2\Lambda_\alpha^2)\right]. \tag{21}$$

As an illustrative example, let us apply the procedure described above to analyze the simplest special case where both side walls of the waveguide are flat. The transformation matrix T is given by

$$\boldsymbol{T} = \boldsymbol{T}_1 \times \boldsymbol{T}_2 \times \cdots \boldsymbol{T}_n \times \cdots \tag{22}$$

$$\boldsymbol{T}_n = \begin{pmatrix} \cos(k_n W) & \sin(k_n W)/k_n \\ -k_n \sin(k_n W) & \cos(k_n W) \end{pmatrix} \tag{23}$$

and

$$k_n^2 = (2\pi/\lambda)^2 - (n\pi/L_g)^2. \tag{24}$$

The eigenvectors

$$\begin{pmatrix} 1 \\ ik_n \end{pmatrix} \text{ and } \begin{pmatrix} 1 \\ -ik_n \end{pmatrix}$$

satisfy the eigenvalue equations

$$\boldsymbol{T}_n \begin{pmatrix} 1 \\ ik_n \end{pmatrix} = \exp(ik_n W) \begin{pmatrix} 1 \\ ik_n \end{pmatrix} \text{ and } T_n \begin{pmatrix} 1 \\ -ik_n \end{pmatrix} = \exp(-ik_n W) \begin{pmatrix} 1 \\ -ik_n \end{pmatrix}$$

as can be easily verified.

For input plane wave from port I with incident angle $= \theta$

$$E_0(x) = \sqrt{2/L_g} \exp\left[ik_0 \sin\theta(x - L_g/2)\right] = E_4^*(x) \tag{25}$$

$$E_3^*(x) = \sqrt{2/L_g} \exp\left[-ik_0 \sin\theta(x - L_g/2)\right]. \tag{26}$$

From (17) and (18) we have

$$S_n = \sqrt{2/L_g} \cdot \int_0^{L_g} \sin(n\pi x/L_g) \exp\left[ik_0 \sin\theta(x - L_g/2)\right] dx \tag{27}$$

$$Q_n = S_n^*. \tag{27a}$$

By straightforward integration, we get

$$S_n = -i1/2\left[\exp(n\pi i/2)\,\mathrm{sinc}\left(k_0 L_g \sin(\theta/2) + n\pi/2\right) - \exp(-n\pi i/2)\,\mathrm{sinc}\left(k_0 L_g \sin(\theta/2) - n\pi/2\right)\right]. \tag{28}$$

Field amplitude as "seen" by the detector at each port can be determined by using (17) and (19) through (21).

The rapid decay of "sinc" function with increasing argument ensures that the infinite sums, over index n and m in the expression for t_4, t_3, r_2, and r_1, have only a few terms (modes) adjacent to $q \simeq k_0 L_g \sin\theta/\pi$ that have significant contribution. Furthermore, the V matrix turns out to be "almost diagonal" (i.e., the elements that are significantly different from zero are those along the diagonal, and in some cases, those adjacent to the diagonal), so that the infinite sum, over index α, also converges rapidly within a few terms in the neighborhood of $\alpha = q$. Most of the energy is thus carried via the mode $q \simeq k_0 L_g \sin\theta/\pi$ and the adjacent modes.

It is the interference between the q mode and adjacent modes which leads to the directivity. In (17), the contribution of the q mode to the sum by product $S_q S_q$ has a magnitude of $\sim 1/2$. The two adjacent modes together contribute 0.405. For t_4, the phase is such that these three modes add, while for t_3 the phase is such that these modes subtract. This picture, in which directivity is a consequence of interference between modes, persists to the case of the diplexer with a curved mirror. For the waveguide with one curved wall, most of the energy comes in two ad-

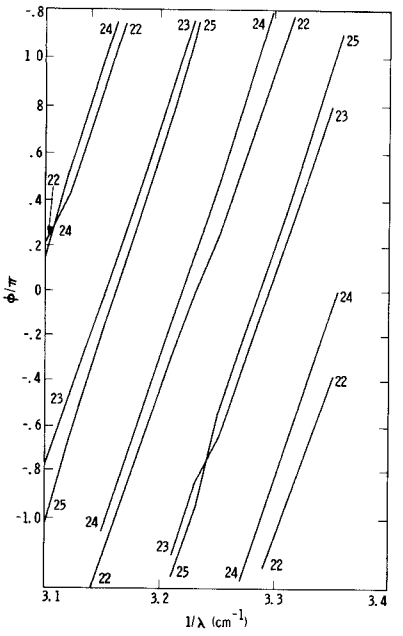

Fig. 6. Phase dispersion of four of the eigenmodes for waveguide with $L = W = 5.28$ cm, $R = 60$ cm.

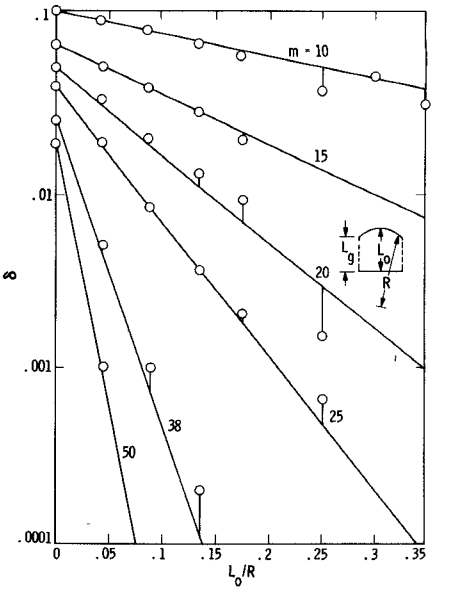

Fig. 7. Normalized phase difference δ of the two dominant eigenmodes versus L_0/R. $m = \sqrt{2}\,L_g/\lambda$ is the resonant order. Straight lines represent the fit by the empirical relation $\delta = \exp(-0.0283\ \mathrm{m}^2/L_0/R)/\mathrm{m}$.

jacent modes with propagation phase factors separated by almost π.

Using parameters for our experimental model with a curved mirror, theoretical phase dispersion curves for four of the eigenmodes have been computed and are plotted in Fig. 6. Note that the eigenmodes are labeled by index q such that $|u_{q\alpha}| \geq |u_{n\alpha}|$ for all n. Although this scheme introduces some ambiguity when two or more basis modes are almost equally dominant, it is convenient because it labels the particular basis mode that has maximum contribution.

Results of our numerical calculations also indicate that, for optimal Gaussian beam input excitation, only two of the eigenmodes are significantly coupled and their phase difference δ turns out to be a crucial parameter that determines the transmission characteristics. We define δ as the fractional part of the phase difference measured in units of π. Equivalently, δ is the frequency separation of the modes divided by the free spectral range. In Fig. 7, values of δ are plotted against L_0/R with $m \equiv 2L_g/\lambda$ as parameters. λ is the free-space wavelength and the meaning of L_0, R, and L_g are defined in the inset for Fig. 7. It is interesting to note that the results (circles) fit very well by the empirical relation $\delta = \exp(-0.0283\ \mathrm{m}^2 L_0/R)/\mathrm{m}$ (straight lines).

Transmission into port IV, $|t_4|^2$, is plotted against input Gaussian beam waist size with radius of curvature of the waveguide as parameter in Fig. 8. The arrows in the figure indicate the waist sizes for which the input Gaussian beam is phase-matched to the curved surface illustrated in Fig. 3. The agreement with our waveguide analysis is excellent.

So far we have completely ignored the existence of metal meshes at the input and output planes or our waveguide. The reflectivity of the metal meshes determine the Finesse F of the diplexer. In practice, values of F are set by system

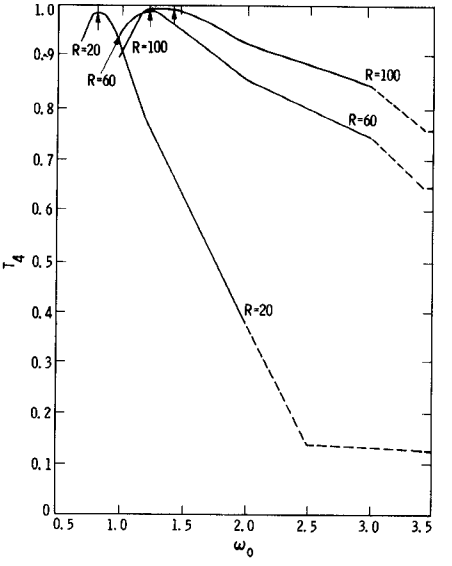

Fig. 8. Through-put (port IV) versus waist size of input Gaussian beam for different wall curvatures. Waist sizes such that the beam phase-matched to the curved surface are indicated by arrows.

requirement. Since the Finesse is the free spectral range in units of transmission linewidth, and δ is the phase difference of the two dominant eigenmodes in units of the free spectral range, the product $F\delta$ can be interpreted as the ratio of phase difference of the two dominant eigenmodes to that of the transmission linewidth. Transmission into port IV, $|t_4|^2$, for diplexers with flat and curved reflectors are compared in Fig. 9 for various values of $F\delta$.

C. Solutions to the Three-Dimensional Problem

To convert the solutions (17), (19), (20), and (21) of the two-dimensional problems into those of the original three-

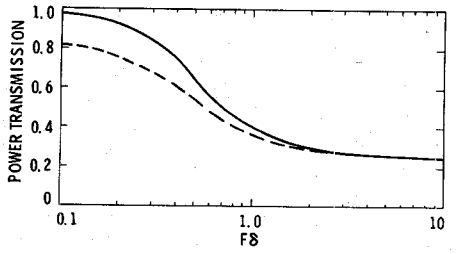

Fig. 9. Transmission (T_4) for diplexers with flat and curved reflectors versus $F\delta$. (——— curved mirror, ---- flat mirror.)

dimensional diplexer problem, we have to consider the effect of finite size and curvature of the walls in the vertical direction. Diffraction loss due to finite size can easily be taken into account simply by replacing the amplitude reflectance r by rf and the amplitude transmittance t by $t\sqrt{f}$, where $1-f$ is the amplitude attenuation per round trip due to vertical diffraction loss. The values of $1-f$ are given in Section III-A. Under the conditions that loss factor is relatively small (i.e., $1-f \ll 1$) and that the vertical curvature of the wall is mild so that the mode structure of the two-dimensional waveguide analyzed in Section III-B is not significantly distorted, the results obtained by this approach should represent a very good approximation to the solutions of the original problem. The effective finesse will be

$$F = \pi(rf)/(1-r^2f^2) \tag{29}$$

and

$$T_4' = T_4(1-r^2)^2 f/(1-r^2f^2)^2 \tag{30}$$

where $T_4 \equiv |t_4|^2$ is the power transmission for port IV of the two-dimensional problem (Fig. 9), and T_4' is the corresponding power transmission for the three-dimensional problem.

IV. Experimental Results

Our experimental setup for transmission measurement in the vicinity of 100 GHz is shown in Fig. 10. Electroformed meshes (MN-40 from Buckbee–Mear Co.) are used as the partially transmitting mirrors at both sides of the diplexer. The monomodal approximation [9] is applied to the free-standing mesh model of Chen [10] to estimate their transmission characteristics. Experimental results at 100 GHz agree fairly well with theory. Experimental values of T_4' (power transmission into port IV) for diplexers with different geometries of reflecting surfaces are compared in Fig. 11. In each case, values of T_4' for the corresponding waveguides (i.e., with no meshes) are used as the 0-dB reference. Note that the peak values of T_4' are improved by steps of approximately 3 dB in going from plane to cylindrical and cylindrical to toroidal reflecting geometries. Within our experimental errors of ± 1 dB, the peak of T_4' for toroidal diplexer shows 0-dB loss relative to the toroidal waveguide. Furthermore, the toroidal geometry also helps in supressing the unwanted secondary transmission peak which invariably appears in the transmission characteristic curves of plane and cylindrical diplexers.

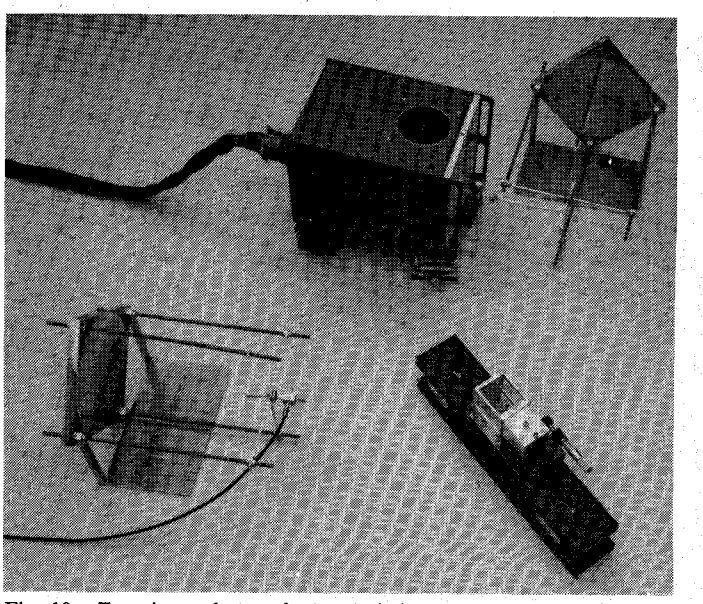

Fig. 10. Experimental setup for transmission measurement in the vicinity of 100 GHz.

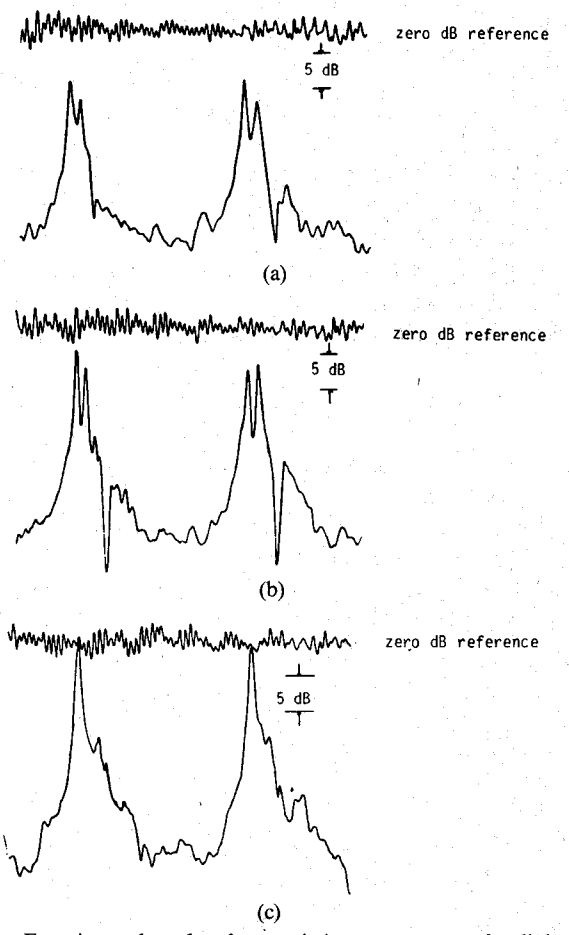

Fig. 11. Experimental results of transmission measurement for diplexers with different geometries. (a) Plane diplexer. (b) Cylindrical diplexer. (c) Toroidal diplexer.

V. Conclusion

In this paper, a solution to the design problem of a folded Fabry–Perot quasi-optical ring resonator diplexer for minimum diffraction effect is given. Performance of diplexers with and without optimal geometry is investigated both theoretically and experimentally. Performance curves are presented so that they can be used to estimate how much improvement in performance one could expect by switching from the plane reflector to the optimal curved reflector.

Important steps are summarized below for the interest of prospective practical users.

1) The size of the cavity, appropriate input Gaussian beam waist size and optimal radii of curvature for minimum diffraction are all determined by the intermediate frequency f_{IF} of the system as explained in Section II.

2) The resonant order q is approximately given by $q = \sqrt{2}\, W/\lambda$.

3) For the plane diplexer, the fractional part of the phase difference of the two dominant eigenmodes in modulo π is given by $\delta \simeq 1/q$.

4) For the toroidal diplexer, the phase difference can be obtained from the empirical formula associated with Fig. 7.

5) Based on the value of the Finesse F required by the experimental condition, peak transmission for both the plane and toroidal diplexers can be estimated from the curves given in Fig. 9, assuming no diffraction loss in the vertical direction.

6) Peak transmission can then be corrected for loss in the vertical direction using (30), and the reflectivity of the mesh can be determined from (29).

Appendix
Determination of T Matrix for a Two-Dimensional Waveguide with One Curved Wall

The basic idea of our approach is to approximate the curved surface by a series of steps as illustrated in Fig. 12. Let the total number of steps be $2N-1$, the depth of the steps are chosen, for later convenience, so that

$$L_i/L_{i-1} = (L_0/L_g)^{1/N} \quad \text{for } i < 0 \tag{A1}$$

$$L_i/L_{i-1} = (L_0/L_g)^{-1/N} \quad \text{for } i > 0. \tag{A2}$$

Note that the ratio is independent of the step index "i". Values of z where the jumps occur are chosen so that the original curve $x(z)$ bisects the vertical segments at each jump, i.e., $x(z_{i-1,i}) = (L_{i-1} + L_i)/2$. The step width W_i is fixed by the conditions above and does depend on the index "i".

The $\boldsymbol{T}$ matrix can be expressed as

$$\boldsymbol{T} = \boldsymbol{P}_N \boldsymbol{T}_d \boldsymbol{P}_{N-1} \boldsymbol{T}_d \cdots \boldsymbol{P}_2 \boldsymbol{T}_d \boldsymbol{P}_1 \boldsymbol{T}_u \boldsymbol{P}_0 \cdots \boldsymbol{P}_{-(N-1)} \boldsymbol{T}_u \boldsymbol{P}_{-N} \tag{A3}$$

where $\boldsymbol{P}_l$, the propagation along step "l" of width δW_l, is

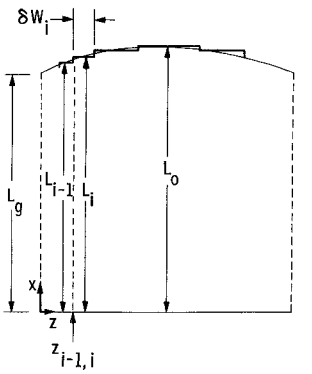

Fig. 12. Approximation of curved wall by steps of constant length ratio.

given by

$$\boldsymbol{P}_l = \boldsymbol{P}_{1l} \times \boldsymbol{P}_{2l} \times \cdots \tag{A4}$$

and

$$\boldsymbol{P}_{nl} = \begin{pmatrix} \cos(k_{nl}\delta_{Wl}) & \sin(k_{nl}\delta W_l)/k_{nl} \\ -k_{nl}\sin(k_{nl}\delta W_l) & \cos(k_{nl}\delta W_l) \end{pmatrix} \tag{A5}$$

with

$$k_{nl}^2 = (2\pi/\lambda)^2 - (n\pi/L_l)^2. \tag{A6}$$

For frequencies beyond cutoff (i.e., for imaginary values of k_{nl}), the expression for k_{nl} given above can still be used with the standard substitution of hyperbolic functions for trigonometric functions.

T_u is the mode change at each "step up jump" given by

$$\boldsymbol{T}_u = \begin{pmatrix} x & 0 \\ 0 & x \end{pmatrix} \tag{A7}$$

and T_d is the corresponding change at each "step down jump" given by

$$\boldsymbol{T}_d = \begin{pmatrix} x^t & 0 \\ 0 & x^t \end{pmatrix} \tag{A8}$$

where

$$x_{mn} = \frac{2}{\sqrt{L_i L_{i-1}}} \int_0^{L_{i-1}} \sin(m\pi x/L_i) \sin(n\pi x/L_{i-1})\, dx$$

$$= \sqrt{L_{i-1}/L_i}\,[\operatorname{sinc}(n\pi - m\pi L_{i-1}/L_i) - \operatorname{sinc}(n\pi + m\pi L_{i-1}/L_i)]. \tag{A9}$$

Note that x_{mn} depends only on n and m, and the ratio L_{i-1}/L_i which is independent of the step index "i".

For the calculations reported here, the step approximation converged when 50 to 100 steps were used. The size of the plane-wave basis required ranged from 10 to 20 values of n centered about q. Only a few waves beyond cutoff could be used because of round-off errors in the cosh and sinh functions.

Acknowledgment

The authors would like to thank N. R. Erikson for stimulating discussions during the early phases of this work.

REFERENCES

[1] J. J. Gustincic, "A quasi-optical radiometer," in *Dig. Second Int. Conf. Submillimeter Waves and Their Applications*, (San Juan, Puerto Rico), Dec. 1976, pp. 106–107.

[2] J. J. Gustincic, "A quasi-optical receiver design," in *IEEE MTT-S Int. Microwave Symp. Dig.*, 1977, pp. 99–101.

[3] See, for example, M. Born and E. Wolf, *Principles of Optics*. New York: Pergamon, 1965.

[4] N. R. Erickson, "A directional filter diplexer using optical techniques for millimeter to submillimeter wavelength," *IEEE Trans. Microwave Theory Tech.*, vol. MTT-25, pp. 865–866, Oct. 1977.

[5] J. A. Arnaud, A. A. M. Saleh, and J. T. Ruscio, "Walk-off effects in Fabry–Perot diplexers," *IEEE Trans. Microwave Theory Tech.*, vol. MTT-22, pp. 486–493, May 1974.

[6] P. F. Goldsmith, "Diffraction loss in dielectric-filled Fabry–Perot interferometers," *IEEE Trans. Microwave Theory Tech.*, vol. MTT-30, pp. 820–823, May 1982.

[7] N. Nakajima and R. Watanabe, "A quasioptical circuit technology for short-millimeter wavelength multiplexers," *IEEE Trans. Microwave Theory Tech.*, vol. MTT-29, pp. 897–905, Sept. 1981.

[8] A. E. Chiou and H. M. Pickett, "Quasi-optical ring resonator diplexer: Theory and experiment," in *Dig. Sixth Int. Conf. Infrared and Millimeter Waves*, Dec. 1981.

[9] S. R. Barone, "Resonances of the Fabry–Perot laser," *J. Appl. Phys.*, vol. 34, pp. 831–843, Apr. 1963.

[10] G. D. Boyd and J. P. Gordon, "Confocal multimode resonator for millimeter through optical wavelength masers," *Bell. Syst. Tech. J.*, vol. 40, pp. 489–508, Mar. 1961.

[11] M. S. Durschlag and T. A. DeTemple, "Far-IR optical properties of freestanding and dielectrically backed metal meshes," *Appl. Opt.*, vol. 20, no. 7, pp. 1245–1251, Apr. 1981.

[12] C. C. Chen, "Transmission through a conducting screen perforated periodically with apertures," *IEEE Trans. Microwave Theory Tech.*, vol. MTT-18, pp. 627–632, Sept. 1970.

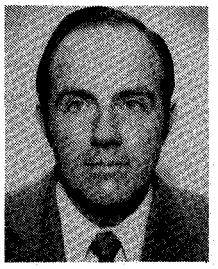

Herbert M. Pickett was born in Baltimore, MD, on April 2, 1943. He received the A.B. degree from Williams College in 1965 and the Ph.D. degree in physical chemistry from the University of California, Berkeley, in 1970. From 1970 to 1973 he was a postdoctoral fellow at Harvard with E. Bright Wilson, Jr. In 1973 he was a Miller Fellow at the University of California.

From 1973 to 1978 he was an Assistant Professor at the University of Texas at Austin. Currently, he is a Research Scientist and Supervisor of Submillimeter Development at the Jet Propulsion Laboratory, California Institute of Technology, Pasadena, CA.

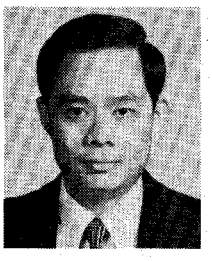

Arthur E. T. Chiou was born in Bassein, Burma, on January 16, 1947. He received the B.Sc. degree in physics from Rangoon Arts and Science University, Rangoon, Burma in 1968, and the M.S. degree in physics from National Taiwan University, Taipei, Taiwan, Republic of China in 1972. He is expected to receive his Ph.D. degree in applied physics from the California Institute of Technology, Pasadena, CA, in June 1983.

He is currently employed at IBM San Jose Research Laboratory.

Numerical Analysis of Open-Ended Coaxial Lines

GREGORY B. GAJDA AND STANISLAW S. STUCHLY, SENIOR MEMBER, IEEE

***Abstract*—Numerical methods are applied in the analysis of coaxial structures used as sensors for *in vivo* permittivity studies of biological substances. The methods used for the solution of the resulting static conductor–dielectric problems are the Finite Element Method (FEM) and the Method of Moments (MOM) applied to a pair of coupled integral equations. A linear model which relates the sample permittivity to the fringing field capacitance of the sensor is discussed and values of the model parameters are calculated for different types of sensors.**

Manuscript received June 25, 1982; revised December 29, 1982. This work was supported by grants from the National Sciences and Engineering Research Council of Canada and Health and Welfare Canada.

The authors are with the Department of Electrical Engineering, University of Ottawa, Ottawa, Ontario, Canada, K1N 6N5.

I. INTRODUCTION

OPEN-ENDED coaxial lines have been used extensively as sensors for permittivity measurements of biological substances in recent years [1]. Their simple geometry and small size (potentially as small as 0.5-mm diameter) makes them suitable for *in vivo* measurements as

0018-9480/83/0500-0380$01.00 ©1983 IEEE